

<https://doi.org/10.1038/s41529-025-00590-x>

# Enhanced hydrogen embrittlement resistance of directed energy deposition 316 L by post-manufacturing heat treatment



Qingyang Liu , Yan Yan, Muhammad Zeeshan Iqbal, Mohammad Tariq, Afrooz Barnoush, Hanan Farhat & Brahim Aissa

This study investigates the hydrogen embrittlement resistance of directed energy deposition additive manufactured 316 L stainless steels with heat treatments. The hydrogen embrittlement sensitivity has been examined through microstructural investigation correlated with grain orientation and dislocation density. The synergistic effect of heat-treatment and hydrogen on strain distribution and instability evolution behavior was revealed. The heat treatment reduced the sub-grain structure and dislocation density, resulting in a more homogeneous microstructure with trace of recrystallization. Hydrogen uptake behavior was closely affected by the microstructure changes and thus hydrogen embrittlement sensitivity was reduced by increasing annealing temperature. AMed samples after heat treatment have a similar hydrogen embrittlement index with conventional manufactured samples. In the heat treated 1200 °C specimens, more strain and instability hotspots were initiated, becoming uniformly distributed and developed. In contrast, the AMed samples initiated fewer strain accumulation sites, which developed into stress/strain concentration areas, leading to wider secondary cracks and ultimate failure.

Research in additive manufacturing (AM) of alloys has attracted increased interest and also made significant developments<sup>1</sup>, particularly in developing high-performance components for harsh environments like nuclear power reactors<sup>2</sup>, aerospace<sup>3</sup>, automotive industry, and hydrogen energy sector<sup>4</sup> and oil refinery applications<sup>5</sup>. The growing popularity of AM production offers the potential to produce complex geometries (functionally grade materials<sup>6</sup>), minimize material waste, and customize parts for specific requirements or repairs<sup>7</sup>. Despite its advantages and superiority, AM still faces many challenges that must be addressed for broader and safer application<sup>5,8,9</sup>, especially hydrogen embrittlement<sup>10–12</sup>. One main obstacle is the limited understanding of the connection between the printing process, optimizing parameters, microstructure, and corresponding mechanical properties<sup>13–15</sup>. Moreover, the scarcity of hydrogen embrittlement data for AMed samples underscores the significance and importance of this study.

Direct energy deposition, also known as DED, is a widely used and versatile method capable of integrating with other manufacturing techniques to create a hybrid process<sup>7,14,15</sup>. While DED allows for the fabrication of heterogeneous materials with preferred properties<sup>7</sup>, the imperfections (like

surface defects and pores) and anisotropic grain structures cannot be ignored<sup>16</sup>. Therefore, post processing heat treatment for DED samples is necessary to relieve residual stress and tailor the microstructure-property relationship<sup>17</sup>. Key objectives of heat treatment include reducing defects and porosity through hot isostatic pressing (HIP), achieving the desired mechanical properties, and enhancing characteristics like high-temperature creep resistance and hydrogen embrittlement resistance.

Many researchers<sup>17–19</sup> have investigated the effect of microstructure changes, such as dislocation, precipitation and low angle grain boundaries, on the mechanical properties, creep behavior and corrosion resistance of as-built 316 L. Y. Li et al.<sup>5</sup> found that the thermal stability of dislocation cell structures, controlled by the chemical micro-segregation, was the dominant factor determining the tensile and creep properties. They<sup>5</sup> also reported that AMed samples have a comparative microstructure and mechanical/creep properties with CMed samples after heat treatment above 1100 °C. However, openly available studies and in-depth analyses are very limited regarding the influence of heat treatments on the HE sensitivity of AMed 316 L. G. Álvarez<sup>20</sup> et al. investigated the combined influence of

post-processing, printing direction, temperature and pre-straining on hydrogen embrittlement susceptibility of AMed 316. They found that heat-treated AM 316 L at 1100 °C may exhibit improved hydrogen compatibility over CM 316 L in cryogenic environments and contributed this improved HE resistance to the reduced propensity of strain-induced martensite formation. L. Claeys et al.<sup>16</sup> also studied the effects of subsequent heat and surface treatments on AMed 316 and found that the trapping sites, dislocation density and residual stress levels were reduced after heat treated at 1066 °C. They<sup>16</sup> found that the oxide layer formed during heat treatment reduced the hydrogen absorption, leading to lower hydrogen solubility and concentration, compared to the higher equilibrium hydrogen concentration at the surfaces of polished samples. The above-mentioned research<sup>16,20</sup> only focused on a specific heat treatment temperature range between 1050 and 1100 °C and failed to provide a wider temperature range (600–1200 °C) and a more in-depth discussion on the improved HE resistance mechanism by heat treatment.

Previous investigation by our group<sup>4</sup> found that the hydrogen embrittlement index of AMed samples was slightly higher than the CMed samples due to the higher dislocation density and higher misorientation angle within the large grains. However, it remains unclear how the combined effects of microstructure evolution, changes in grain size, and the reduced trapping sites induced by heat treatment influence hydrogen uptake, diffusion, and hydrogen-induced cracking behavior in AMed samples. In this study, we systematically investigated the microstructural evolution of AMed 316 and its effects on hydrogen embrittlement performances after heat treatments at different temperatures. Observations of in-situ strain evolution were performed on tensile-tested samples, both hydrogen free (HF) and hydrogen charged (HC), before and after heat treatments. We introduced digital image correlation as a pioneering method to track the onset and development of strain/instability at microscale, enhancing the correlation between microstructure and tensile behavior. The results from this study will help fill the gap in understanding how increased heat treatment temperatures affect the hydrogen embrittlement behavior of additively manufactured stainless steel 316.

## Results

### Microstructure evolution with annealing temperature

Figure 1 shows the cellular microstructural evolution of L-DED samples with different annealing temperatures. These images were taken at three magnifications from optical microscopy and SEM. The as-deposited sample has a characteristic structure of overlapping layers and a periodic array of deposition tracks/melting pools<sup>21</sup>, which were highlighted by dashed red and black lines in Fig. 1 (a1). It was reported that the high cooling rate during AMed-DED process derived the ‘cubes’ microstructure on AD samples<sup>9</sup>. As shown in Fig. 1 (a2) and (a3), hexagonal and elongated cellular structures were found on the AD samples, consisting of the equiaxed and dendrite grains. It is worth noting that the cellular structures in samples began to dissolve after annealing at 600 °C and completely disappeared after annealing at 1200 °C. After heat treatment at 600 °C and 800 °C, the melting pool became less visible, and the cellular grains grew larger compared to AD samples. Recrystallized grains were found in Fig. 1 (b3), (c3) and (d3), as indicated by black arrows. The cellular structures in AMed samples were reported to exhibit prominent thermal stability up to 600 °C<sup>17,22</sup>, as the cellular walls started to vanish and decompose after annealing at 600 °C. At 800 °C, the overall cellular structure became less visible in Fig. 1 (c3), while the dislocations started to disentangle<sup>5</sup> within cell walls<sup>17</sup>. After heat treatment at 1200 °C, the cellular structures were eliminated completely, as shown in Fig. 1 (d1–d3). Literature suggests that a homogeneous microstructure is expected to form, and dislocation cells also disappear at annealing temperatures above 1000 °C<sup>5,17</sup>. As shown in Fig. 1 (d2–d3), the microstructure reveals entirely different equiaxed grains without sub-grain structures, alongside the presence of annealing twins, indicating that recrystallization has occurred<sup>17</sup>. As shown in Fig. 1 (a3–d3), pores were typical microstructure of AMed samples and were visible on all the samples, indicating that heat treatment without proper Hot Isostatic Pressing cannot eliminate these pores.

For further examination of orientation and morphology evolution of the grains, EBSD analyses were carried out for samples before and after each heat treatment. Figure 2a, b show the inverse pole figures and corresponding grain reference misorientation maps. The statistical grain sizes obtained from Fig. 2c are 41.2, 26.7, 28.4, 47.3 μm for AD, HT-600, HT-800 and HT-1200 samples, respectively. The misorientation angle was found to decrease with increasing annealing temperature, as shown in Fig. 2b, d. We found a highly heterogeneous microstructure characterized by a higher misorientation angle at the grain boundaries (GBs) of AD sample in Fig. 2(a1, b1). Small recrystallization regions with lower misorientation angles were found in HT-600 and HT-800 samples, indicated by black circles in Fig. 2 (a2 & a3) and (b2 & b3). After annealing at 1200 °C, there is a significant increase in grain size, accompanied by characteristic annealing twin boundaries, as shown in Fig. 2 (a4 and b4), indicating the activation of recrystallization at this temperature. This is aligned with the work reported in ref. 17, where the microstructure shows near defect-free grains with annealing twins and a decrease in LAGBs. Li<sup>5</sup> reported the thermal stability of dislocation cells is directly linked to the recrystallization ability<sup>22</sup>. In this study, the thermal stability of dislocation cells remains stable up to 600 °C, with notable recrystallization occurring at this temperature and above.

### Dislocation density measurement by XRD

The samples consist of single austenite phase when annealed at temperatures below 1200 °C, as indicated by XRD results shown in Fig. 3a. Ferrite was detected in samples annealed at 1200 °C, which agrees with the refs. 9,23,24. Other researchers<sup>25,26</sup> reported a whole single austenite phase in L-PBF samples regardless of the annealing temperature. It should be noted that the phase transformation of ferrite in austenitic stainless steels depends on many factors such as heterogeneities of as-built materials, cooling rate after heat treatment and the chemical composition (ratio of Cr/Ni) of the alloy<sup>17,25</sup>. The possibility of ferrite formation is suppressed by the combined effect of a low Cr/Ni ratio and high dislocation density, the latter resulting from the rapid solidification during the process<sup>25,26</sup>. As reported in the literature, dislocation density is significantly reduced after high temperature annealing<sup>23,27</sup>, making phase transformation much more likely to occur.

Following rapid cooling during AMed-DED process, the unstable dislocation structure, caused by the retained excess energy, can be alleviated through post-heat treatment via homogenization and recrystallization<sup>22,23</sup>. The density of dislocation can be calculated by Williamson-Hall equation<sup>28</sup>, which correlates the relationship between  $\delta_{hkl} \cos\theta_{hkl}/\lambda$  and  $4\sin\theta_{hkl}/\lambda$  by measuring the full width at half-maximum (FWHM) of the four peaks corresponding to (111), (200), (220) and (311) reflections, taken from Fig. 3a<sup>4</sup>. Figure 3b presents the linear relation between  $\delta_{hkl} \cos\theta_{hkl}/\lambda$  and  $4\sin\theta_{hkl}/\lambda$ , as well as the corresponding linear fit. By estimating the line slope of each sample, the dislocation densities for AD, HT600, HT800 and HT1200 were calculated to be  $11.22 \times 10^{13} \text{ m}^{-2}$ ,  $4.89 \times 10^{13} \text{ m}^{-2}$ ,  $3.69 \times 10^{13} \text{ m}^{-2}$ , and  $1.58 \times 10^{13} \text{ m}^{-2}$  respectively. After heat treatment, the dislocation density decreased monotonically with increasing temperature, consistent with ref. 17, which reported a reduction in lattice strain and FWHM at annealing temperatures of 600 °C and above.

To further validate the above result from XRD, TEM analysis was conducted to assess the dislocation distribution and density, as shown in Fig. 4, where the dislocations appear as dark lines in bright field image. The as-received sample showed a high density of uniformly distributed dislocations throughout the sample, while HT1200 sample showed fewer visible dislocations, which were distributed sporadically. To quantify dislocation density, the TEM images were processed by image segmentation method from Image Processing Toolbox in MATLAB. The images were converted to grayscale and then segmented based on its grayscale intensity level using adaptive threshold method, separating dark (dislocation) and light pixels. And the dislocation ratio was calculated as the area percentage of dark pixels. As shown in Fig. 4 insets, the as-received sample exhibited a higher dislocation ratio of 20.61%, compared to 9.5% for HT1200 sample. The intercept method<sup>29</sup>

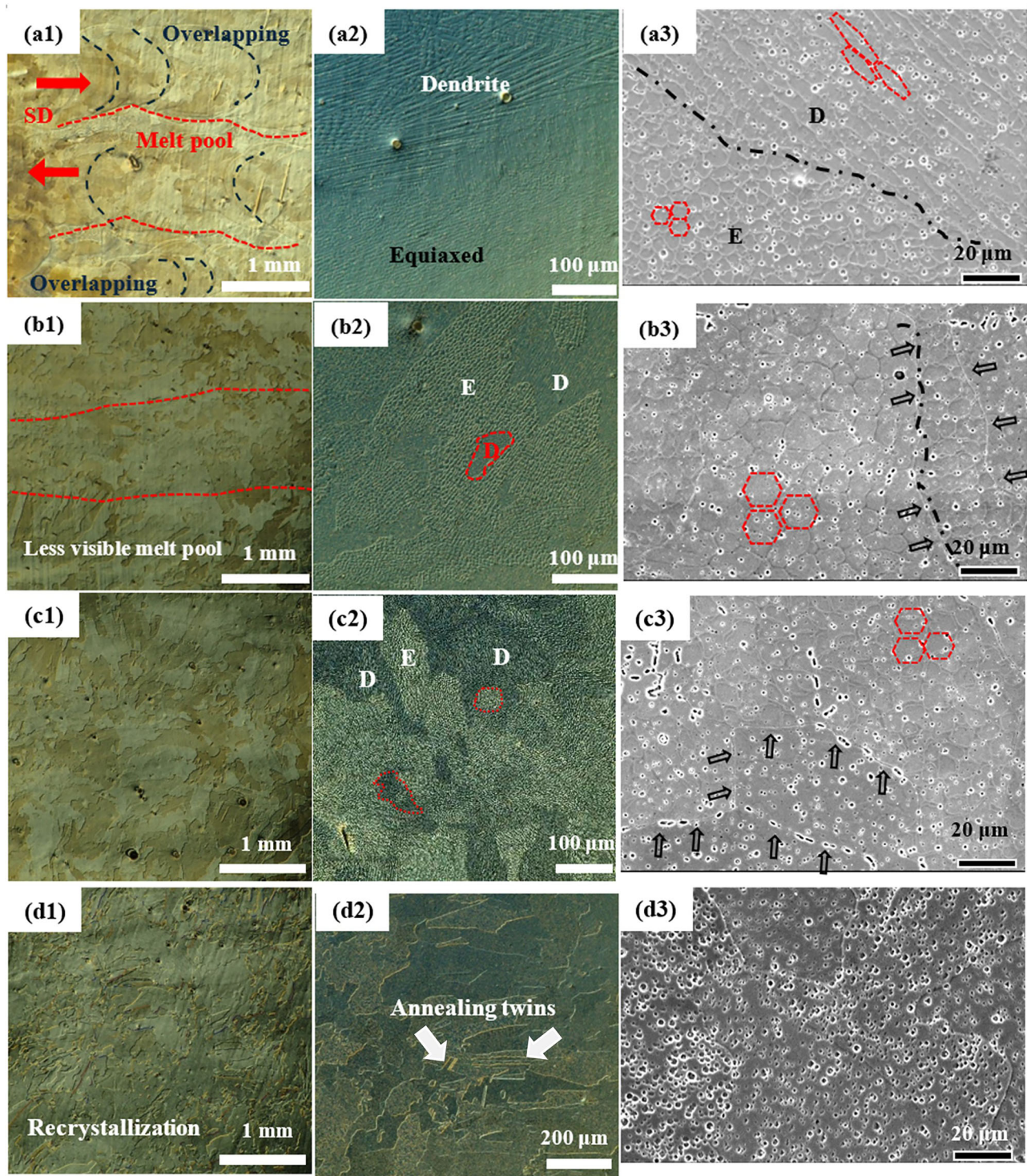


**Fig. 1 | Optical and SEM micrographs.** a as-DED material and as-DED specimens heat treated at (b) 600 °C (HT-600), (c) 800 °C (HT-800), (d) 1200 °C (HT-1200), the built direction is out of plane. abbreviation 'D' and 'E' stands for 'dendrite and

equiaxed' respectively. The dashed lines in (a3–c3) means the growth of cellular structure. Pores from the manufacturing process were always visible in (a3–d3).

was also performed on the TEM segmented images, the dislocation density value for AD and HT1200 samples were calculated to be  $14.9 \times 10^{13} \text{ m}^{-2}$  and  $2.9 \times 10^{13} \text{ m}^{-2}$ , respectively. It should be noted that the dislocation difference is much larger than what the ratio indicates, as the dislocation image in Fig. 4b was taken from a surface where the dislocations were distributed randomly. The effect of dislocation density on the hydrogen uptake and mechanical properties will be further discussed in this paper.

### Mechanical properties and hydrogen embrittlement behavior

**Mechanical behavior.** Tensile tests were conducted at room temperature for hydrogen free (HC) and hydrogen charged (HC) as-deposit samples and heat-treated samples at different annealing temperatures. It was found the engineering stress-strain curve was not changed significantly with printing direction<sup>30</sup>. So, in this study, one building direction was chosen for the hydrogen embrittlement test for consistency. Three repetitive tests were performed for each condition, and the average

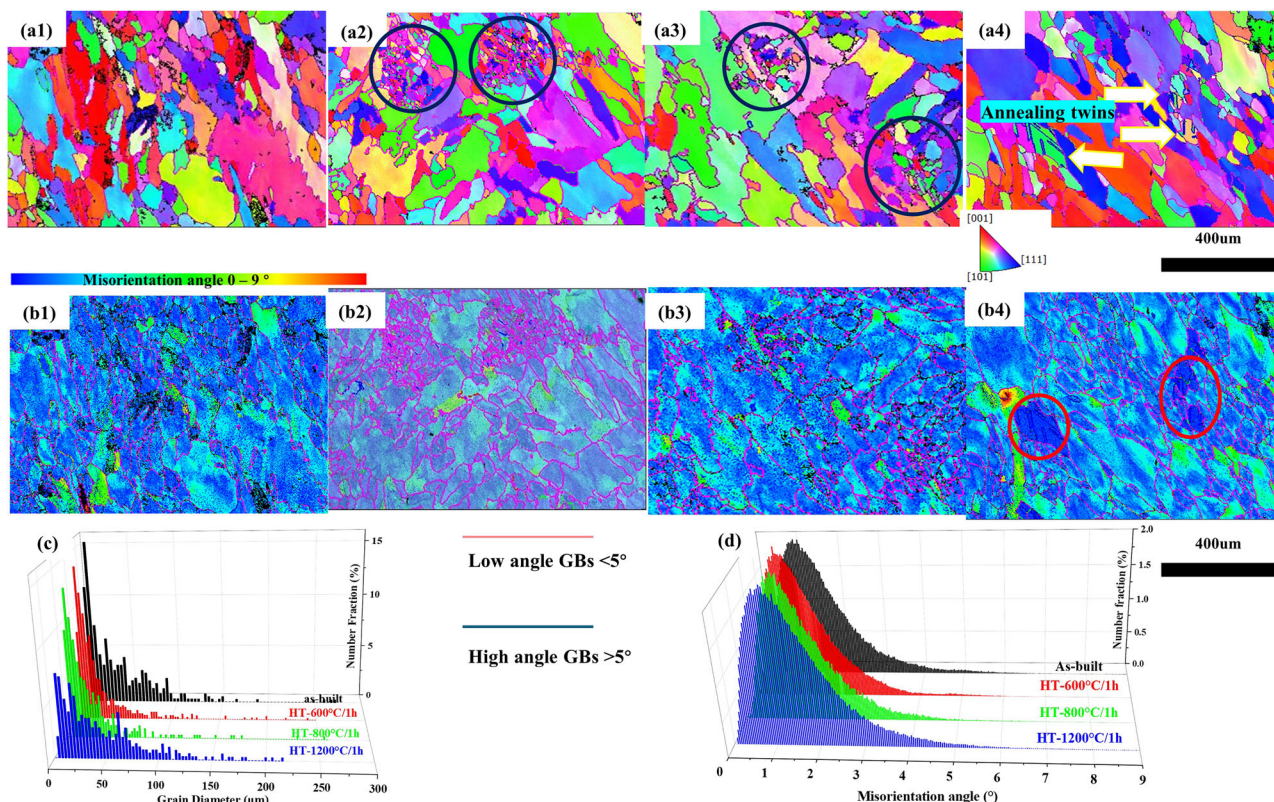


**Fig. 2 | EBSD images and misorientation maps.** Effect of heat treatment temperature on the microstructure. **a** EBSD Inverse Pole Figure grain orientation maps for each material condition: (a1) as-DED, as-DED specimens heat treated at (a2) 600 °C, (a3) 800 °C, (a4) 1200 °C. **b** Misorientation distribution map with angle for

corresponding AMed samples (number assignment for b is same with a). **c, d** Grain diameter and misorientation angle map, respectively. Low and high angle GBs are highlighted with different GB line colors. (For interpretation of the references to color in this figure legend, the reader is referred to the Web version of this article.).

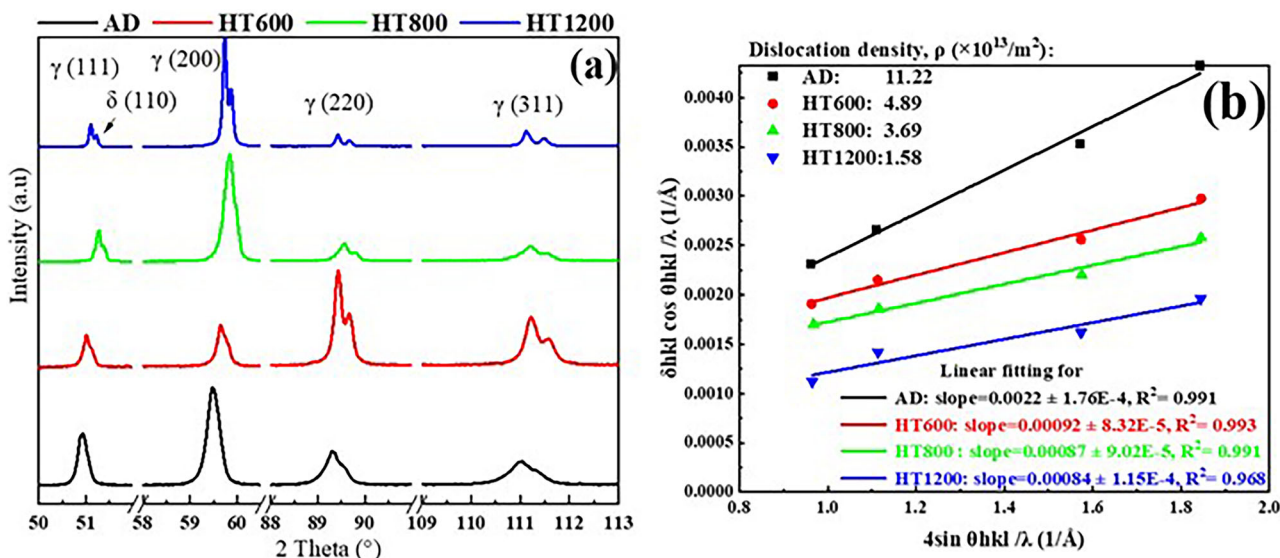


**Fig. 3 | XRD details for calculating dislocation density.** **a** XRD spectra of studied AMed samples with different heat treatments (left); **b** Dislocation density measured by XRD (right).

value of tensile strength, strains and HEI was plotted in Fig. 5. The detailed raw data can be found in Supplementary Information. The test with the closest result to the average value was deliberated selected as the representative case in this study for further digital image correlation and the sequent test/figures. Figure 6a, b show this representative engineering and true stress-strain curve, respectively. Table 1 summarized this

representative tensile properties and hydrogen embrittlement index as function of annealing temperature.

For hydrogen-free conditions, the yield strength decreased slightly for all heat-treated samples, but ultimate tensile strength increased when annealing at temperature above 800 °C. The lower yield strength of heat-treated samples with smaller grain sizes is also surprisingly different than

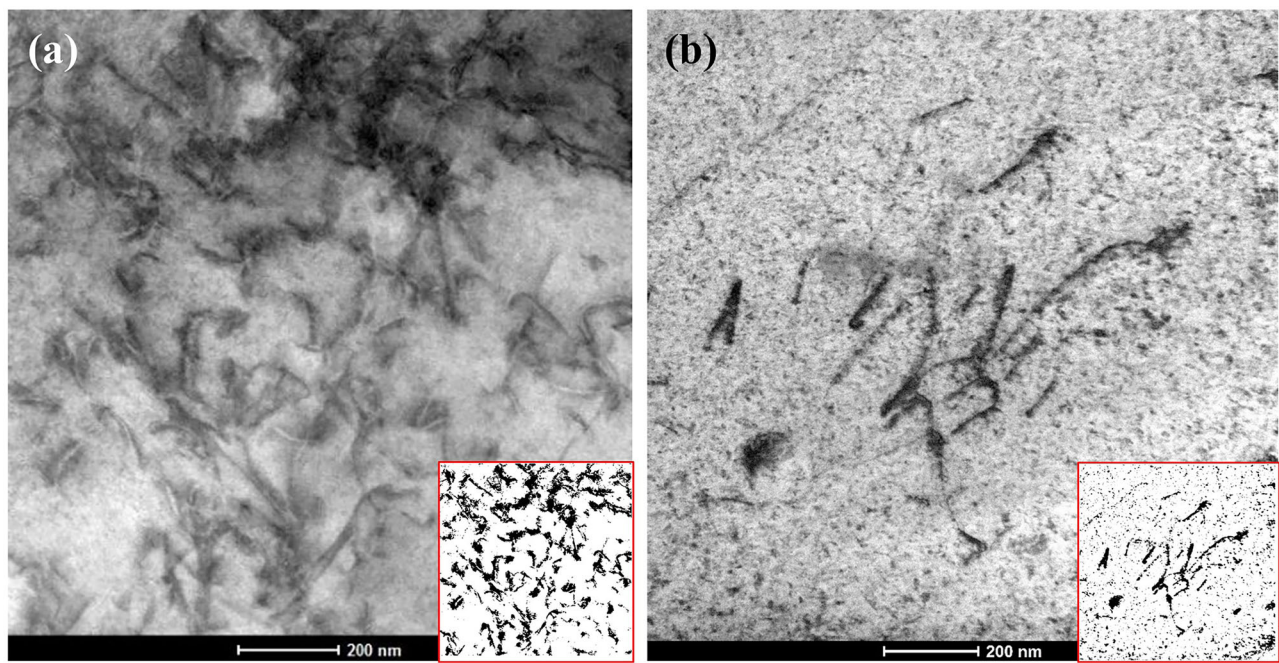
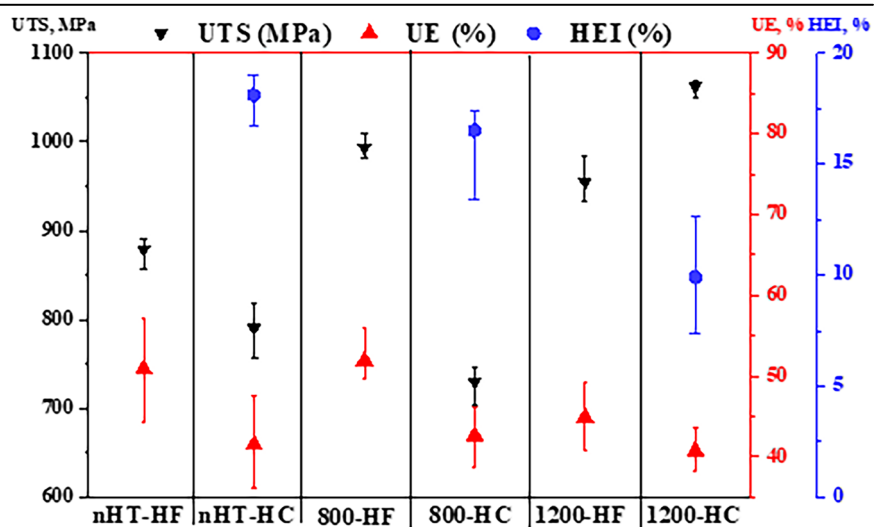


**Fig. 4 | Dislocation measurement from TEM.** **a** as-received sample with a dislocation area percentage of 20.61%, and **(b)** HT-1200 sample with a reduced dislocation area percentage of 9.50%. Right-bottom insets are the segmented images highlighting dislocation regions for clearer visualization.

**Fig. 5 | Summary of the tensile strength, ultimate elongation and HEI results from three repetitive tests (detailed data can be found in the supplementary information).**



what is expected from the Hall-Petch effect<sup>4,17</sup>. The decrease of yield strength after heat treatment was due to the dislocation rearrangement<sup>5</sup>. The slight increase of elongation was only observed in the HT-800 sample. The classic strength-ductility trade-off behavior is not obvious due to the serrated drops during the tensile tests. AMed samples in this study exhibited better mechanical properties than those reported in the literature<sup>5,16,17,20,30</sup>. The combination of strength and elongation for hydrogen free samples showed a slight increase after heat treatment at 800 °C and 1200 °C<sup>17,23</sup>. In contrast, the decrease of strength and elongation for the HT-600 sample may be attributed to the sensitization behavior of stainless steels<sup>31</sup>. The increase in grain size can also be attributed to the changes in mechanical properties of heat-treated samples, suggesting the grain boundary unpinning effect of particles<sup>32</sup>. The Vickers Microhardness test was performed on hydrogen-free heat-treated samples, and the results are shown in Fig. 6d. The microhardness of the as-DED sample was around 215 HV, which agrees

with ref. 4. The microhardness decreased continuously from 193HV to 188HV as the annealing temperature increased from 600 to 1200 °C, a trend reported to be related to ferrite formation<sup>8</sup> and residual stress release<sup>24</sup>. However, they<sup>24</sup> also found a slight increase of microhardness to 200 HV after heat treatment at 1400 °C, due to the twinning structure formation that hinders the dislocation glide. The decrease of hardness is also linked to the reduction in dislocation density as the annealing temperature increases<sup>22</sup>, which has been confirmed by the XRD results and other literature<sup>17,33</sup>.

**Enhance Hydrogen embrittlement resistance by heat treatment.** The mechanical properties of hydrogen charged samples exhibited reduced ductility compared to hydrogen free samples at all heat treatment conditions, as shown in Fig. 6a. The corresponding hydrogen desorption curve (from TDS) and hydrogen content after tensile test was measured on the crack tip and shown in Fig. 6c. Heat treated samples at 1200 °C

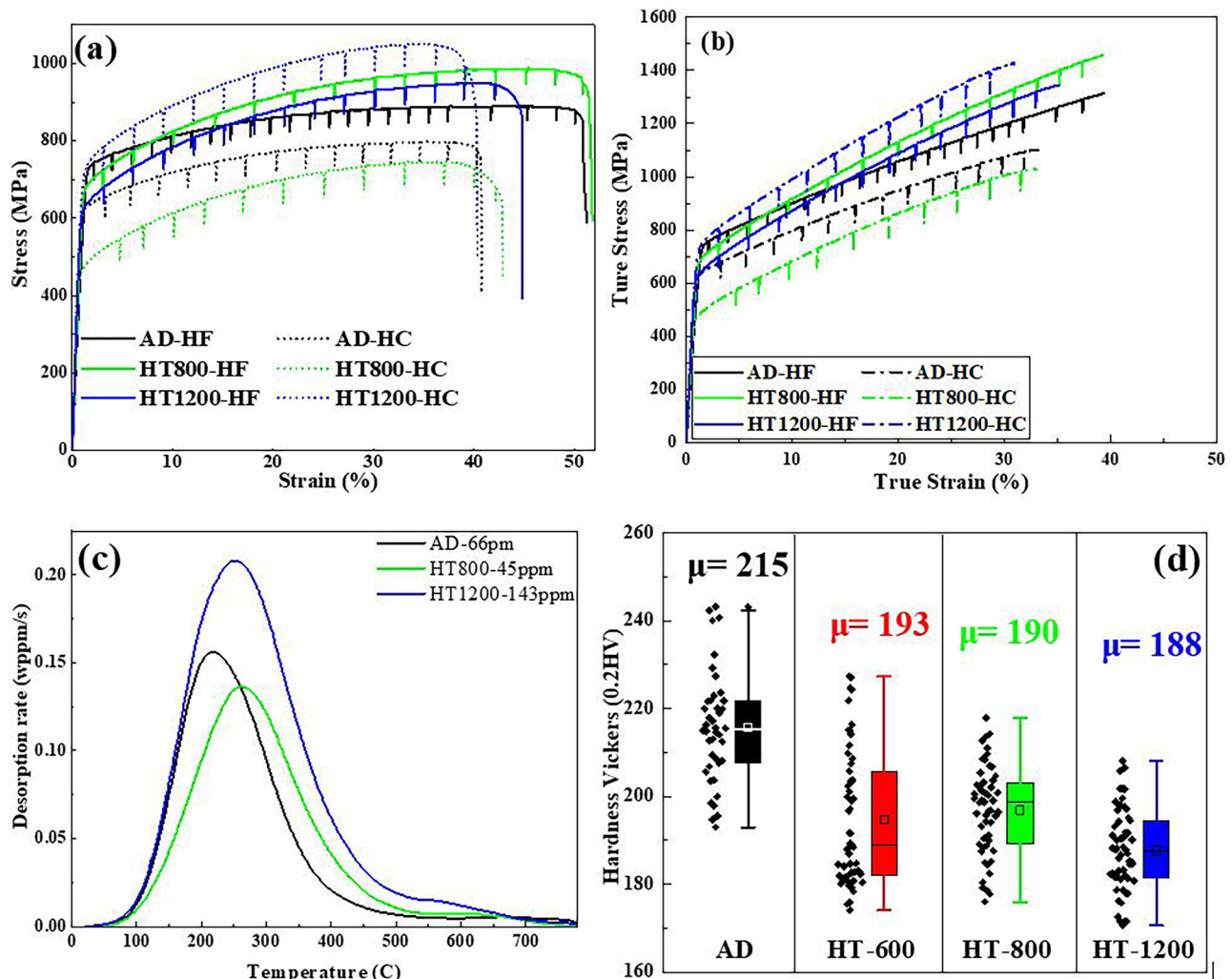


**Fig. 6 | Mechanical properties.** **a, b** Engineering and True tensile Stress-strain relationships for AMed samples as a function of heat treatment temperature and hydrogen charging. **c** Hydrogen desorption curve for AMed samples with different heat treatment. **d** Vickers Microhardness test results on hydrogen free samples with different heat treatment.

**Table 1 | Summary of the values for offset yield strength (OYS), ultimate tensile strength (UTS), ultimate (total) elongation (UE), hydrogen concentration ( $C_H$ ) and HEI of as-DED and heat-treated specimens with/without hydrogen charging**

Condition	OYS(MPa)	UTS(MPa)	UE(%)	CH(wppm)	HEI (%)
AD-HF	696	890	51.0	-	-
AD-HC	610	797	41.1	66.1	19.4
HT800 °C-HF	658	985	51.1	-	-
HT800 °C-HC	451	746	42.8	45.3	16.2
HT1200 °C-HF	611	950	44.8	-	-
HT1200 °C-HC	690	1051	40.3	143	10.0

The result is for 'the' representative test.

indicated an increased tensile strength after hydrogen charging<sup>4,16</sup>. The AD sample may trap more hydrogen than HT800 sample due to its higher dislocation density<sup>4</sup>. The highest hydrogen concentration (143 ppm) was found in HT1200 sample, where an increased number of twin grain boundaries likely served as hydrogen trapping sites<sup>11</sup>. The stress-strain curve in Fig. 6a was used to calculate the loss of ductility (so-called hydrogen embrittlement index, HEI), where a higher HEI indicates a higher susceptibility to HE<sup>4</sup>. It should be noted that the HEI is usually calculated based on area reduction, but this method was not used in this study due to the sample geometry limitation<sup>4,16</sup>. The HEI of tested

samples were summarized in Table 1, and HEI decreased from 19% for AD sample to 16% and 10% after heat treatment at 800 and 1200 °C, regardless of the hydrogen concentration. The HT1200 sample exhibited the best hydrogen embrittlement resistance even with the highest hydrogen concentration. It is reasonable to conclude that the elimination of cell walls by heat treatment can markedly improve hydrogen resistance.

**Fracture observation.** To better understand how heat treatment influences the tensile properties and hydrogen embrittlement behavior of the AMed 316SS samples, the fracture morphology was performed using SEM and shown in Fig. 7. Special attention was given to the surface secondary cracks and the fracture mode at the sample edge, where the hydrogen diffusion was limited by the depth, resulting in a hydrogen concentration gradient as predicted by the previous modelling calculation<sup>30</sup>. The necking behavior with visible slip lines were found on the fracture of hydrogen-free samples at all heat treatment conditions, as shown in Fig. 7 (a1–d1). The fracture showed a typical ductile mode with dimples for all hydrogen free samples, as shown in Fig. 7 (b1–b4).

In comparison, hydrogen charged samples exhibited the brittle fracture mode without necking. As shown in Fig. 7 (a3–d3), parallel secondary cracks were observed on the surface near the fracture due to the presence of hydrogen reduced the stacking fault energy in AMed samples<sup>34,35</sup>. Only intergranular corrosion was found on the fracture of HT-600 samples and no brittle fracture zone was found on the other heat treated hydrogen

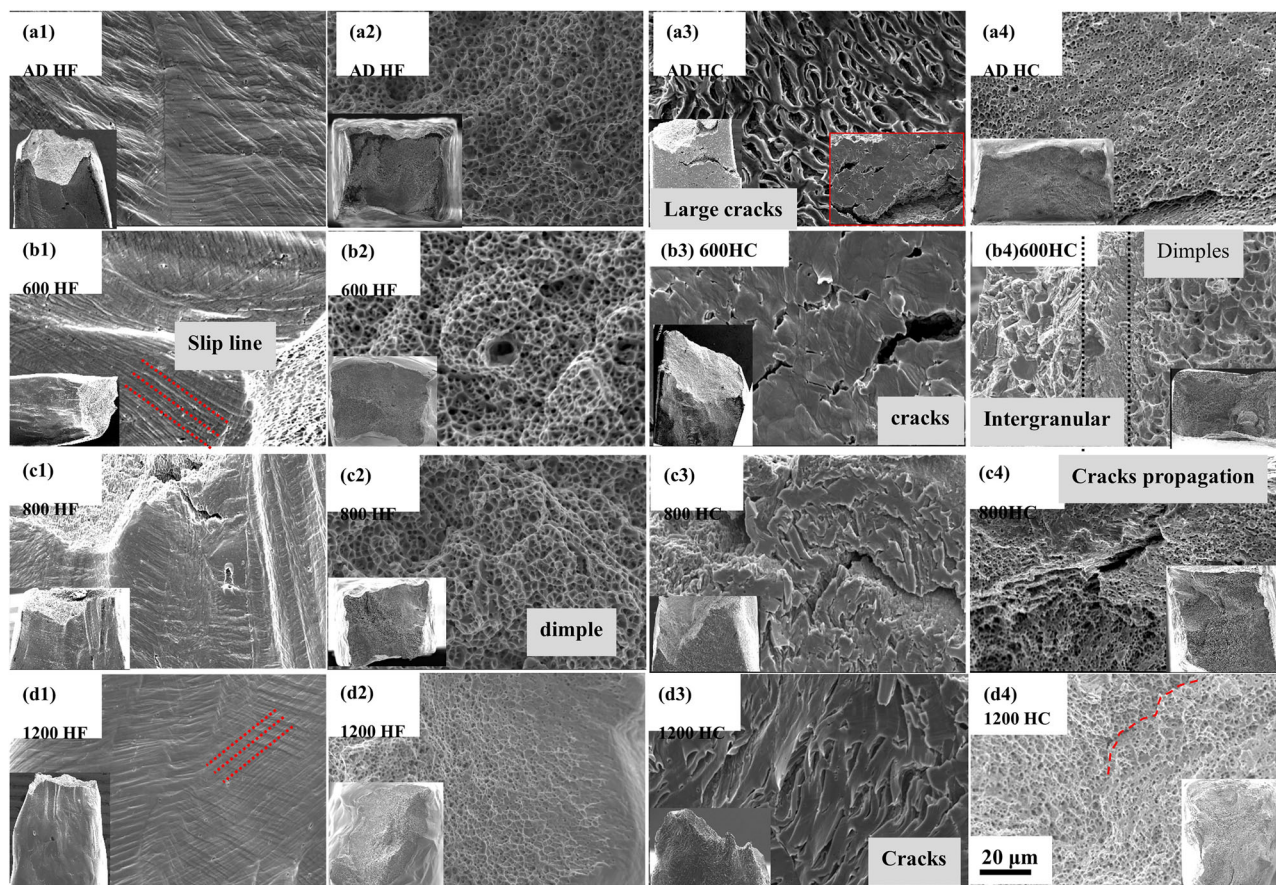


**Fig. 7 | SEM surface and fracture observation.** For samples before and after hydrogen charging on (a) AD, (b) HT600, (c) HT 800 and (d) HT1200, scale bar is shown in d4.

charged samples, which agrees with the ref. 16. Heat treatment at 600 °C could introduce the effect of sensitization, increasing the hydrogen embrittlement index, as confirmed by the observed intergranular corrosion<sup>31</sup>.

## Discussion

Results from this study indicate that the mechanical behavior and hydrogen embrittlement resistance of AMed samples are dependent on the hydrogen concentrations and post-process conditions, especially heat treatment temperature. The following discussion will summarize how heat treatment affects the microstructure and dislocation density with different annealing temperatures. The improved hydrogen embrittlement resistance will then be evaluated, with specific attention on the interaction between hydrogen and microstructure. The in-situ digital image correlation results on the strain distribution will conclude these effects on the tensile tests.

### Microstructure evolution with annealing temperature

Heat treatment at different temperatures reveals notable microstructural diversification, as shown in Fig. 1. Compared to as-deposit (AD) samples, deposition tracks/melting pool/sub-grains structure gradually faded, with a more pronounced crystallization changes becoming visible as the annealing temperature increased<sup>17</sup>. Y. Li et al. also revealed that the recrystallization and grain refinement<sup>36</sup> occurred in DED-316L, which were promoted by heat treatment at temperatures exceeding the recrystallization threshold of 750 °C. The average grain size also remained stable up to 800 °C.

Except for the thermal stability of sub-grain structure and recrystallization occurrence, dislocation density was also remarkably affected by the heat treatment temperature<sup>4</sup>. The decrease of FWHM from XRD results in Fig. 3a indicates a reduction elastic lattice strain and dislocation density with increasing annealing temperature. T. Voisin<sup>17</sup> et al. also reported that the reduced lattice strain and dislocation density was attributed to the

homogenization and residual stress changes. As is well known, the microstructure is closely related to the mechanical properties of the samples. The combined effects of recrystallization and reduced dislocation density resulted in higher tensile strength and elongation at an annealing temperature of 800 °C, as shown in Fig. 6a. The recrystallized twinning grains and grain boundaries (shown in Fig. 1 d1 and Fig. 2 a4) hindered the motion of dislocation<sup>37</sup>, and thus improved the tensile strength but reduced the elongation of HT-1200 sample. It was reported that the strength-ductility relationship was compromised by introducing the dislocation network<sup>32</sup>, which pre-existed and acted as a ‘modulator’ that slowed down but did not completely block the motion of dislocation. This dislocation network can keep its stability until heat treatment at 1200 °C, with the disappearance of the sub-grain structure (Fig. 1 d1–d3) and the decrease of dislocation density (Fig. 3b).

### Elevated hydrogen embrittlement resistance via heat treatment

The hydrogen embrittlement behavior of the samples was also affected by heat treatment. The most obvious impact at first was the hydrogen uptake behavior of the samples after different heat treatments. The hydrogen atoms diffused into the steel and were trapped at various internal sites, including lattice sites, dislocations, grain boundaries, and precipitates<sup>4,16,38</sup>. Different dislocation density, grain boundary types and other structure characteristics directly influence the hydrogen uptake behavior of the studied samples. As deposited sample with higher dislocation density trapped more hydrogen (66 ppm) than HT-800 sample (45 ppm), and HT-1200 sample trapped most hydrogen (143 ppm) even with lowest dislocation density. This is due to the formation of twin grains & GBs during recrystallization process, which provided additional lattice sites for hydrogen trapping.

Reduced dislocation density in HT-800 samples resulted in a lower hydrogen trapping capability and lower hydrogen concentration. As the temperature exceeded the recrystallization temperature, the dislocation

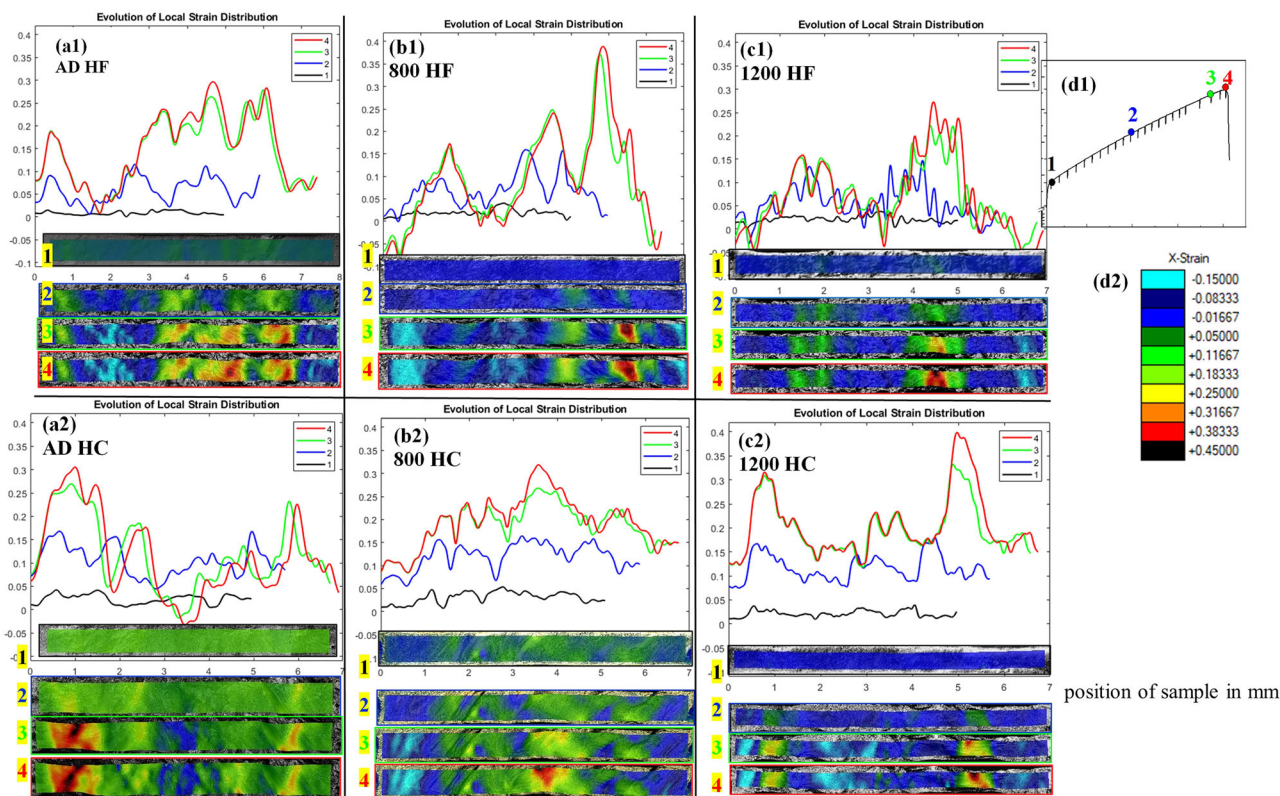


**Fig. 8 | Strain distribution maps.** Evolution of local strain distribution of (a) as-deposit, (b) HT-800 and (c) HT-1200 samples with and without hydrogen charging. Average values of the local strain distribution are shown for 4 selected holding points (at different tensile stages, explicating in (d1)). These points are illustrated in the tensile curve in (d1), corresponding to critical deformation stages: 1 near the yield

strength, 2 middle of the uniform elongation, 3 approaching the ultimate tensile strength and 4 immediately before the fracture. The color -code strain scale was shown in (d2). x-axis is the horizontal position (tensile direction) along the sample in mm from left to right and y-axis is the corresponding x-strain values (calculated as the mean strain along the vertical direction at each horizontal position).

density of HT-1200 sample remained as low as that of HT-800 sample but exhibited a higher amount of lattice sites and twins GBs for trapping hydrogen. This explains the higher hydrogen concentration in HT-1200 samples. The columnar dendrites were reported to hinder the diffusion of hydrogen<sup>39</sup>, which is the main reason that lower hydrogen content was found for AD, HT800 samples. AD sample was most susceptible to HE with a highest HEI and HT-1200 sample exhibited lowest HEI despite having the highest hydrogen concentration. It is reasonable to conclude that the hydrogen trapped in the dislocations contributed more to reducing the ductility of samples. To distinguish the hydrogen reversible and irreversible trapped sites, a common method is to correlate the hydrogen desorption peak temperature with the heating rate from TDS curve<sup>28,33</sup>. As shown in Fig. 6 c, the hydrogen trapping sites (lattice sites, dislocation and grain boundaries) are all reversible (also called diffusible) trapping sites<sup>28,33</sup>, with a desorption peak at below 300 °C.

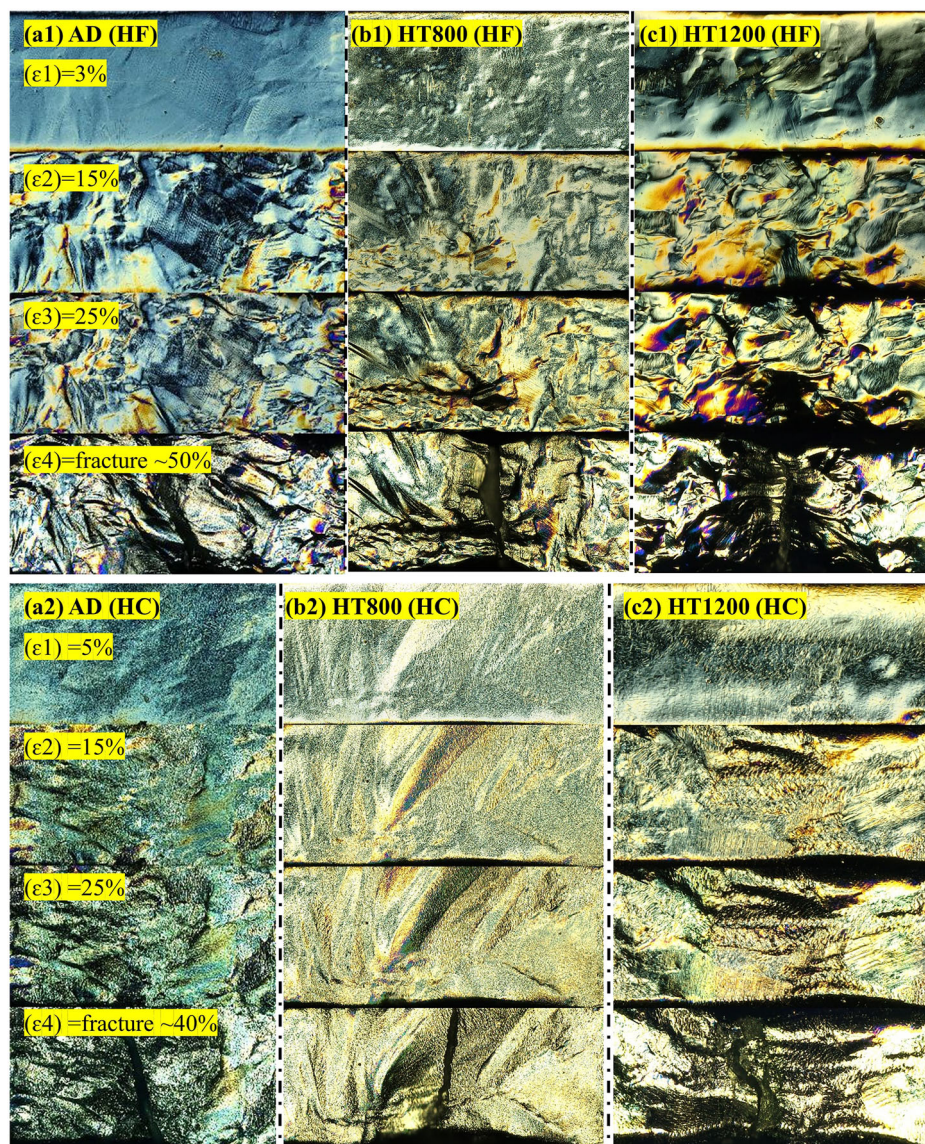
### In-situ strain dynamic evolution from Digital image correlation

To better understand the effect of hydrogen charging on the fracture behavior of AMed samples before and after different heat treatment, the representative local strain distribution and its evolution for samples at different strain stages was depicted in Fig. 8. Figure 8 (d1) shows the DIC results at different holding points at specific strain, holding point 1 is near the yield strength, holding point 2 is the middle of the uniform elongation, holding point 3 is approaching the ultimate tensile strength and holding point 4 represents the strain just before the fracture. The color-coded x-strain distribution of the gauge part and local strain distribution curves are shown in Fig. 8. In the strain curves, x-axis is the horizontal position (tensile direction) along the sample in mm from left to right and y-axis is the corresponding x-strain values (calculated as the mean strain along the vertical direction at each horizontal position). It is worth noting that as the image size increased

with sample elongation, a shift of strain distribution curve was observed. Images focusing on a small region of interest (ROI) around the crack area were captured at different strain values and are shown in Fig. 9.

For hydrogen free samples, there is no obvious strain variation at stage 1 (black lines) near the yield strength, indicating uniform deformation regardless of heat treatment conditions or the presence of hydrogen. More attention has been given to the strain nucleation and growth from stage 2 to stage 3, where the deformation behavior of samples is significantly affected by heat treatment and hydrogen uptake. More strain/instability peaks were observed on heat-treated samples than non-heat-treated samples, as shown in Fig. 8 (a1–c1). Three main strain sites (strain > 0.1) were found on AD-samples at stage 2 and these strain peaks are growing to stage 3 without formation of new strain/instability sites. This is due to the higher density of dislocation and larger grain size in AD samples. Strain and deformation accumulated around local defects/grain boundaries under applied stress, eventually growing and evolving into the primary cause of failure. A similar trend was found on HT-800 sample, whose deformation behavior exhibited three main strain sites at stage 2 and eventually developed to a final fracture strain value. More than ten major strain/instability sites (strain value > 0.1) were initiated on HT-1200 sample by loading from stage1 to stage 2, indicating a uniform plastic instability occurring on the sample surface during the tensile test. From the discussion above, we found that the microstructural changes of HT-1200 sample, characterized by the formation of twin grains and a reduction in dislocation density, led to decreased anisotropy, which is closely related to the microstructural alternation induced by heat treatment<sup>36</sup>. As a result, strain/instability initiated and propagated uniformly across the surface, as shown in Fig. 8 (c1). Two hot-spot regions were found at the stage 3 and 4 for HT-1200 sample and the necking phenomenon was observed on the fracture in Fig. 9 (c1), which is typical fracture behavior for conventionally manufactured 316 L<sup>4</sup>. The sample after

**Fig. 9 | Small region of interest.** Cracking area for (a) as-deposit, (b) HT-800 and (c) HT1200 sample at (1): hydrogen free and (2): 24 h hydrogen charging conditions. (3%,15%,25% and fracture strain).



heat treatment at 1200 °C has comparable tensile properties and fracture behavior to CMed sample.

For hydrogen charged samples, the strain/instability distribution behavior of samples before and after different heat treatments are shown in Fig. 8 (a2–c2). Additionally, detailed fracture observations within small ROI are shown in Fig. 9 (a2–c2). Compared to hydrogen free samples, intensified strain fluctuation was found in the hydrogen charged samples at stage 1. Notably, the strain/instability nucleated and initiated on hydrogen charged samples at stage 1 can grow and develop into stage 2 and 3, exhibiting a markedly different behavior compared to hydrogen free samples. Also, there is no formation of new instability region during tensile test between stage 1 and stage 2. Results indicated that the hydrogen had an immediate effect at the very beginning of tensile test and this effect persisted until fracture, which can be contributed to the hydrogen uptake behavior during hydrogen charging process. The hydrogen accumulation behavior at specific areas of the pre-charged samples established the strain/instability distribution map. It is well established that H atoms can accumulate around dislocations, leading to a phenomenon known as ‘dislocation pinning’ effect and making it harder for dislocations to move<sup>39,40</sup>, which in turn affects the material’s ductility and can make it more susceptible to brittle fracture. Compared to the visible slip lines in hydrogen free samples, the secondary cracks observed in fracture morphology shown in Fig. 7 (a3–d3) and Fig. 9 (a2–c2)

confirmed that the presence of hydrogen induced a more brittle fracture and reduced the ductility. It was reported that the H atom in the stacking fault plane can weaken the interaction between the Fe atoms of the interlayers, and lead to more secondary cracks by reducing the stacking fault energy<sup>34,35</sup>.

This study has investigated and compared the hydrogen embrittlement behavior of DED Additive manufactured stainless steel 316 L after different heat treatments. This includes the mechanism of how HE resistance can be enhanced via post-process treatments. The major findings can be concluded as follows. Heat treatment (at 600 °C, 800 °C, and 1200 °C) resulted in notable microstructural changes: cellular structures were progressively destroyed, and recrystallization occurred, particularly at 1200 °C. This change promoted the development of equiaxed grains with annealing twins, further contributing to enhanced mechanical properties and HE resistance. The dislocation density decreased with increasing annealing temperatures, which directly influenced hydrogen uptake, solubility and trapping behavior. Higher dislocation density in as-deposited samples provides more hydrogen trapping sites. And formation of twin grain boundaries and other lattice sites in samples treated at 1200 °C showed a higher HE resistance even with higher soluble hydrogen concentration. The heat treatments at 800 °C and 1200 °C enhanced both tensile strength and elongation for hydrogen-free samples, breaking the typical strength-ductility trade-off of conventional manufacturing materials. Hydrogen-charged samples showed more

**Table 2 | Chemical composition (in wt. %) of the as-deposited L-DED 316 L SS**

Element	C	Mn	Si	N	Cr	Ni	Mo	Al	Fe
AD-316L	0.008	1.43	0.38	0.02	18.8	12.5	2.81	0.05	64.2

brittle fractures with secondary cracks, confirming the H atom weakens the stacking fault energy of the Fe atom interlayers. Digital image correlation (DIC) was pioneered to reveal heat-treated samples exhibited more uniform plastic deformation and strain instability initiation across the surface. Strain initiated at the hydrogen accumulation sites in hydrogen charged samples and developed toward the final failure zone.

## Methods

### Material and heat treatment

316 L SS samples were deposited by COMTED FHT via Laser-Directed Energy Deposition (L-DED)<sup>5</sup> system equipped with a 2 kW ytterbium fiber laser source<sup>36</sup>. A set of L-DED process parameters and building protocol can be found in previous paper<sup>4</sup>. The chemical composition of the as deposited 316 L SS was measured via glow discharge optical emission spectroscopy, as shown in Table 2. The DED deposited samples were annealed at different temperatures (600, 800, and 1200 °C) with a heating rate of around 20 °C/min in an argon-flowing furnace for 1 h, followed by furnace cooling to room temperature. Then flat dog-bone tensile specimens with gauge dimensions of 5 mm (length) × 1 mm (width) × 1 mm (thickness) were prepared for hydrogen charging and tensile test.

### Tensile test on hydrogen charged sample

The detailed hydrogen charging process can be found in our previously published paper<sup>4</sup>. The cathodic hydrogen charging was carried out in a mixed glycerol and phosphoric acid solution at 75 °C under potentiostatic control at −2000 mV (equal to a current density of 50 mA/cm<sup>2</sup>) to preserve a corrosion-free surface. A Platinum mesh was used as a counter electrode, Ag/AgCl was used as a reference electrode and two identical samples were connected to the working electrode. After 24 h hydrogen charging, twin samples were carefully rinsed with de-ionized water and ethanol, then dried with compressed air in preparation for subsequent Thermal Desorption Spectroscopy (TDS) and tensile testing, respectively. The processing time was strictly limited to 10 min to avoid hydrogen desorption. TDS (Bruker G4 PHONIX DH) was used to measure the hydrogen concentration in the samples at a heating rate of 20 °C/min from room temperature to 800 °C.

Tensile tests were performed on hydrogen charged and hydrogen free specimens to investigate the hydrogen embrittlement susceptibility using a miniature tensile module (Kammrath & Weiss GmbH) with a 50 kN load. Three parallel samples were tested to ensure the repeatability of the results. The tensile direction is parallel to the scanning direction and perpendicular to the building direction. Samples were deformed at a constant strain rate of 0.001 s<sup>−1</sup> under high resolution optical microscope (Olympus DSX 1000) in Differential Interference Contrast mode. The tensile test was briefly paused at every 150 μm elongation intervals to capture images, continuing until sample fracture. These images were stitched using automatic panorama stitching with a 10% overlap. Images of the gauge part of samples were taken for further Digital Image Correlation (DIC) analysis by Ncorr MATLAB<sup>44</sup>. DIC tracks the relative displacement of material patterns between undeformed (reference image) and deformed images. The parameters for DIC analysis are: subset radius of 30–50 pixels, subset spacing of 5 pixels, strain radius of 8 pixels, and pixel density of 1–1.25 pixel/μm. The detailed description can be found in previous publication<sup>4</sup>. Additionally, a small region of interest (ROI) around the final failure area was highlighted to trace the changes in surface topography after a specific amount of strain.

According to ASTM E92-17, microhardness measurements were performed on heat-treated samples without hydrogen using a INNOVATEST Nemesis 5102 Universal Hardness Tester, under a load of 200 gf for 15 s with a distance between indentations of 500 μm. As the hydrogen hardening effect,

attributed to the hydrogen enhanced dislocation density, has been previously reported<sup>4</sup>, this study focuses solely on the effect of heat treatment on the evolution of hardness, independent of hydrogen influence. Hardness values were calculated from the diagonal length of indentations according to standard EN ISO 6507: Vickers hardness =  $0.1891 \cdot F / d^2$ , where F is testing force in newtons (N) and d is arithmetic mean of two diagonal lengths in mm.

### Microstructure characterization

AD and heat-treated DED 316 L SS specimens were examined on the planes perpendicular to the build direction to better understand the link between mechanical properties and microstructure. The samples were prepared by mechanical grinding, polishing, electropolishing and 1 min electrochemical etching in 10% oxalic acid for microstructure analysis. The electropolishing was conducted in a solution of 1 M methanolic H<sub>2</sub>SO<sub>4</sub> solutions at 25 V for 35 s at room temperature. Characterization of the material grain structure was performed via scanning electron microscope (SEM, JEOL 6610LV, Japan) equipped with energy-dispersive spectroscopy system (EDS AZtecOne, Oxford Instruments Group, England) and an electron backscatter diffraction (QUANTAX EBSD, Bruker, Germany) system with accelerating voltage at 20 kV. X-ray diffraction (XRD, Rigaku, Japan) was also performed at ambient temperature using monochromatic Co K $\alpha$  radiation ( $\lambda = 1.789 \text{ \AA}$ ) at 40 kV and 20 mA to identify the microstructural phases of the studied samples. The diffraction patterns were collected over a  $2\theta$  range of 40° to 120°, with a step size of 0.1° and a count time of 15 s/step.

Transmission electron microscopy (TEM) was performed on as received and HT1200 samples to characterize the dislocation distribution and quantify its density as supporting evidence for XRD results. TEM samples were cut using Focused Ion Beam (FIB) and coated with platinum before micro-machining the samples to ~100 nm thick for TEM analysis. The TEM analysis was performed using a Thermo Scientific TalosF200X TEM and a FEI TECNAI G2 FEG TEM, operating at 200 keV to obtain bright-field and STEM-HAADF images.

### Data availability

Data is provided within the manuscript or supplementary information files.

Received: 31 October 2024; Accepted: 17 April 2025;

Published online: 27 May 2025

## References

- Melzer, D., Džugan, J., Koukolíková, M., Rzepa, S. & Vavřík, J. Structural integrity and mechanical properties of the functionally graded material based on 316L/IN718 processed by DED technology. *Mater. Sci. Eng.: A* **811**, 141038. <https://doi.org/10.1016/j.msea.2021.141038> (2021).
- Maziasz, P. J. & Busby, J. T. In *Comprehensive Nuclear Materials* (ed Rudy J. M. Konings) 267–283 (Elsevier, 2012).
- Gisario, A., Kazarian, M., Martina, F. & Mehrpouya, M. Metal additive manufacturing in the commercial aviation industry: A review. *J. Manuf. Syst.* **53**, 124–149. <https://doi.org/10.1016/j.jmsy.2019.08.005> (2019).
- Liu, Q. et al. Influence Of Hydrogen Uptake on Additively Manufactured and Conventional Austenitic Stainless Steels 316L. *Mater. Sci. Eng.: A*, 147170. <https://doi.org/10.1016/j.msea.2024.147170> (2024).
- Li, Y., Krajňák, T., Podaný, P., Veselý, J. & Džugan, J. Thermal stability of dislocation structure and its effect on creep property in austenitic 316L stainless steel manufactured by directed energy deposition. *Mater. Sci. Eng.: A* **873**, 144981. <https://doi.org/10.1016/j.msea.2023.144981> (2023).
- Shah, K. et al. Parametric study of development of Inconel-steel functionally graded materials by laser direct metal deposition. *Mater. Des.* (1980-2015) **54**, 531–538. <https://doi.org/10.1016/j.matdes.2013.08.079> (2014).
- Ahn, D.-G. Directed Energy Deposition (DED) Process: State of the Art. *Int. J. Precis. Eng. Manuf.-Green. Technol.* **8**, 703–742. <https://doi.org/10.1007/s40684-020-00302-7> (2021).

8. Rodrigues, T. A. et al. Effect of heat treatments on 316 stainless steel parts fabricated by wire and arc additive manufacturing: Microstructure and synchrotron X-ray diffraction analysis. *Addit. Manuf.* **48**, 102428. <https://doi.org/10.1016/j.addma.2021.102428> (2021).
9. Saboori, A., Piscopo, G., Lai, M., Salmi, A. & Biamino, S. An investigation on the effect of deposition pattern on the microstructure, mechanical properties and residual stress of 316L produced by Directed Energy Deposition. *Mater. Sci. Eng.: A* **780**, 139179. <https://doi.org/10.1016/j.msea.2020.139179> (2020).
10. Liu, Q. et al. *Eff. prestrain Hydrog.-Induc. delayed Crack. medium Mn steels* **29**, 1929–1938 (2020).
11. Liu, Q. et al. The effect of hydrogen concentration on the fracture surface of medium Mn steels. *Eng. Fail. Anal.* **108**, 104263. <https://doi.org/10.1016/j.engfailanal.2019.104263> (2020).
12. Liu, Q. et al. *Eff. Relat. Humidity Mech. Degrad. Medium Mn Steels* **13**, 1304 (2020).
13. Baek, S.-W. et al. Hydrogen embrittlement of 3-D printing manufactured austenitic stainless steel part for hydrogen service. *Scr. Materialia* **130**, 87–90. <https://doi.org/10.1016/j.scriptamat.2016.11.020> (2017).
14. Yoo, J. et al. Investigation of hydrogen embrittlement properties of Ni-based alloy 718 fabricated via laser powder bed fusion. *Int. J. Hydrog. Energy* **47**, 18892–18910. <https://doi.org/10.1016/j.ijhydene.2022.04.045> (2022).
15. Kevinsanny et al. Defect tolerance and hydrogen susceptibility of the fatigue limit of an additively manufactured Ni-based superalloy 718. *Int. J. Fatigue* **139**, 105740. <https://doi.org/10.1016/j.ijfatigue.2020.105740> (2020).
16. Claeys, L., Deconinck, L., Verbeken, K. & Depover, T. Effect of additive manufacturing and subsequent heat and/or surface treatment on the hydrogen embrittlement sensitivity of 316L austenitic stainless steel. *Int. J. Hydrog. Energy* **48**, 36142–36157. <https://doi.org/10.1016/j.ijhydene.2023.05.215> (2023).
17. Voisin, T. et al. New insights on cellular structures strengthening mechanisms and thermal stability of an austenitic stainless steel fabricated by laser powder-bed-fusion. *Acta Materialia* **203**, 116476. <https://doi.org/10.1016/j.actamat.2020.11.018> (2021).
18. Wang, Y., Voisin, T. & McKeown, J. et al. Additively manufactured hierarchical stainless steels with high strength and ductility. *Nature Mater* **17**, 63–71 (2018).
19. Margulies, L., Winther, G. & Poulsen, H. F. In Situ Measurement of Grain Rotation During Deformation of Polycrystals. **291**, 2392–2394. <https://doi.org/10.1126/science.1057956> (2001).
20. Álvarez, G., Harris, Z., Wada, K., Rodríguez, C. & Martínez-Pañeda, E. Hydrogen embrittlement susceptibility of additively manufactured 316L stainless steel: Influence of post-processing, printing direction, temperature and pre-straining. *Addit. Manuf.* **78**, 103834. <https://doi.org/10.1016/j.addma.2023.103834> (2023).
21. Smith, T. R., Sugar, J. D., San Marchi, C. & Schoenung, J. M. Microstructural development in DED stainless steels: applying welding models to elucidate the impact of processing and alloy composition. *J. Mater. Sci.* **56**, 762–780. <https://doi.org/10.1007/s10853-020-05232-y> (2021).
22. Deng, P. et al. On the Thermal Stability of Dislocation Cellular Structures in Additively Manufactured Austenitic Stainless Steels: Roles of Heavy Element Segregation and Stacking Fault Energy. *JOM* **72**, 4232–4243. <https://doi.org/10.1007/s11837-020-04427-7> (2020).
23. Liu, L. et al. Dislocation network in additive manufactured steel breaks strength–ductility trade-off. *Mater. Today* **21**, 354–361. <https://doi.org/10.1016/j.mattod.2017.11.004> (2018).
24. Saeidi, K., Gao, X., Lofaj, F., Kvetková, L. & Shen, Z. J. Transformation of austenite to duplex austenite-ferrite assembly in annealed stainless steel 316L consolidated by laser melting. *J. Alloy. Compd.* **633**, 463–469. <https://doi.org/10.1016/j.jallcom.2015.01.249> (2015).
25. Salman, O. O., Gammer, C., Chaubey, A. K., Eckert, J. & Scudino, S. Effect of heat treatment on microstructure and mechanical properties of 316L steel synthesized by selective laser melting. *Mater. Sci. Eng.: A* **748**, 205–212. <https://doi.org/10.1016/j.msea.2019.01.110> (2019).
26. Shamsujjoha, M., Agnew, S. R., Fitz-Gerald, J. M., Moore, W. R. & Newman, T. A. High Strength and Ductility of Additively Manufactured 316L Stainless Steel Explained. *Metall. Mater. Trans. A* **49**, 3011–3027. <https://doi.org/10.1007/s11661-018-4607-2> (2018).
27. Bertsch, K. M., Meric de Bellefon, G., Kuehl, B. & Thoma, D. J. Origin of dislocation structures in an additively manufactured austenitic stainless steel 316L. *Acta Materialia* **199**, 19–33. <https://doi.org/10.1016/j.actamat.2020.07.063> (2020).
28. Shi, R. et al. Atomic-scale investigation of deep hydrogen trapping in NbC/ $\alpha$ -Fe semi-coherent interfaces. *Acta Materialia* **200**, 686–698. <https://doi.org/10.1016/j.actamat.2020.09.031> (2020).
29. Gallet, J. et al. Experimental measurement of dislocation density in metallic materials: A quantitative comparison between measurements techniques (XRD, R-ECCI, HR-EBSD, TEM). *Mater. Charact.* **199**, 112842. <https://doi.org/10.1016/j.matchar.2023.112842> (2023).
30. Li, Y., Podany, P., Salvetti, P., Brázda, M. & Džugan, J. Building rate effect on microstructure and high temperature mechanical properties of Austenitic 316L stainless steel manufactured by laser directed energy deposition. *Opt. Laser Technol.* **172**, 110535. <https://doi.org/10.1016/j.optlastec.2023.110535> (2024).
31. Liu, Q. et al. Application of double loop electrochemical potentiokinetic reactivation for characterizing the intergranular corrosion susceptibility of stainless steels and Ni-based alloys in solar nitrate salts used in CSP systems. *Eng. Fail. Anal.* **129**, 105717. <https://doi.org/10.1016/j.engfailanal.2021.105717> (2021).
32. Hu, J., Chen, B., Smith, D. J., Flewitt, P. E. J. & Cocks, A. C. F. On the evaluation of the Bauschinger effect in an austenitic stainless steel—The role of multi-scale residual stresses. *Int. J. Plasticity* **84**, 203–223. <https://doi.org/10.1016/j.iijplas.2016.05.009> (2016).
33. Luo, Y., Li, W., Jiang, L., Zhong, N. & Jin, X. Hydrogen embrittlement and hydrogen diffusion behavior in interstitial nitrogen-alloyed austenitic steel. *Int. J. Hydrog. Energy* **46**, 32710–32722. <https://doi.org/10.1016/j.ijhydene.2021.07.084> (2021).
34. Barnoush, A. & Vehoff, H. J. A. M. Recent developments in the study of hydrogen embrittlement: Hydrogen effect on dislocation nucleation. **58**, 5274–5285 (2010).
35. Hermida, J. D. & Roviglione, A. Stacking fault energy decrease in austenitic stainless steels induced by hydrogen pairs formation. *Scr. Materialia* **39**, 1145–1149. [https://doi.org/10.1016/S1359-6462\(98\)00285-1](https://doi.org/10.1016/S1359-6462(98)00285-1) (1998).
36. Li, Y., Koukolíková, M., Džugan, J. & Brázda, M. High temperature fracture behavior of 316L stainless steel-Inconel 718 functionally graded materials manufactured by directed energy deposition: Role of interface orientation and heat treatment. *Mater. Sci. Eng.: A* **898**, 146389. <https://doi.org/10.1016/j.msea.2024.146389> (2024).
37. Matsumoto, R. & Taketomi, S. Molecular dynamics simulation of Surface-Adsorbed-Hydrogen-Induced Dislocation Motion in a thin film. *Computational Mater. Sci.* **171**, 109240. <https://doi.org/10.1016/j.commatsci.2019.109240> (2020).
38. He, Y., Su, Y., Yu, H. & Chen, C. First-principles study of hydrogen trapping and diffusion at grain boundaries in  $\gamma$ -Fe. *Int. J. Hydrog. Energy* **46**, 7589–7600. <https://doi.org/10.1016/j.ijhydene.2020.11.238> (2021).
39. Yu, H. et al. Hydrogen Embrittlement as a Conspicuous Material Challenge—Comprehensive Review and Future Directions. *Chem. Rev.* **124**, 6271–6392. <https://doi.org/10.1021/acs.chemrev.3c00624> (2024).
40. Behvar, A., Haghshenas, M. & Djukic, M. B. Hydrogen embrittlement and hydrogen-induced crack initiation in additively manufactured metals: A critical review on mechanical and cyclic loading. *Int. J. Hydrog. Energy* **58**, 1214–1239. <https://doi.org/10.1016/j.ijhydene.2024.01.232> (2024).

41. Blaber, J., Adair, B. & Antoniou, A. Ncorr: Open-Source 2D Digital Image Correlation Matlab Software. *Exp. Mech.* **55**, 1105–1122, <https://doi.org/10.1007/s11340-015-0009-1> (2015).

## Acknowledgements

The study was supported by Qatar Environment and Energy Research Institute (QEERI) by Qatar Foundation, Qatar. The authors acknowledge the funding and support from Qatar National Research Fund for the program ‘3D Printed hydrogen resistant alloys: Unlocking the evolution of hydrogen energy in Qatar’ (Grant No. NPRP14S-0324-210091). Special gratitude to Dr. Brahim Aissa for the kindly help through the revision process. The authors thank the HBKU Core Labs Team for material characterizations. Dedicated to Dr. Hanan Alshareef Farhat for her contribution to the corrosion center in QEERI. Open Access funding is provided by Qatar National Library.

## Author contributions

Q.L. Writing – review & editing, Writing – original draft, Resources, Methodology, Investigation, Formal analysis, Data curation, Conceptualization. Y.Y. Writing – review & editing, Software, Formal analysis. M.I. Formal analysis, Data curation. M.T. Investigation, Writing – review & editing, Software, Data curation. A.B. Writing – review & editing, Supervision, Software, Resources, Methodology, Formal analysis, Data curation. H.F. Writing – review & editing, Supervision, Resources, Project administration, Methodology, Funding acquisition, Investigation. B.A. Writing – review & editing, Supervision, Resources, Project administration. All authors reviewed the manuscript.

## Competing interests

The authors declare no competing interests.

## Additional information

**Supplementary information** The online version contains supplementary material available at <https://doi.org/10.1038/s41529-025-00590-x>.

**Correspondence** and requests for materials should be addressed to Qingyang Liu or Brahim Aissa.

**Reprints and permissions information** is available at <http://www.nature.com/reprints>

**Publisher's note** Springer Nature remains neutral with regard to jurisdictional claims in published maps and institutional affiliations.

**Open Access** This article is licensed under a Creative Commons Attribution 4.0 International License, which permits use, sharing, adaptation, distribution and reproduction in any medium or format, as long as you give appropriate credit to the original author(s) and the source, provide a link to the Creative Commons licence, and indicate if changes were made. The images or other third party material in this article are included in the article's Creative Commons licence, unless indicated otherwise in a credit line to the material. If material is not included in the article's Creative Commons licence and your intended use is not permitted by statutory regulation or exceeds the permitted use, you will need to obtain permission directly from the copyright holder. To view a copy of this licence, visit <http://creativecommons.org/licenses/by/4.0/>.

© The Author(s) 2025